The Evolution of Agricultural Drought Transition Periods in the U.S. Corn Belt

NICHOLAS J. SCHIRALDI AND PAUL E. ROUNDY

Department of Atmospheric and Environmental Sciences, University at Albany, State University of New York, Albany, New York

ABSTRACT

Agricultural drought in the U.S. Corn Belt region (CBR) has tremendous global socioeconomic implications. Unfortunately, the weather and climate factors that contribute to transition events toward or away from such droughts are poorly understood. This study applies composite, trajectory clusters, and a vertically integrated moisture budget to understand the phenomena that influence transition events that evolve over 20 and 60 days as modulated by interannual, intraseasonal, and synoptic-time-scale variability during May–August over the CBR. Results show that a shift in the low-frequency base state does not explain onset or decay of the 20- or 60-day drought transition cases. Instead, amplification of an intraseasonal Rossby wave train across the Pacific Ocean into North America, which occurs coincident with intraseasonal tropical convection on its equatorward side, triggers the transition. Trajectory analysis reveals similar source regions for air parcels associated with drought development and breakdown, but with a shift toward more parcels originating over the Gulf of Mexico during transitions away from drought. Finally, the vertically integrated moisture budget shows that advection and convergence of moisture on intraseasonal time scales dominates during these transitions. These results demonstrate that weather events are the primary driver of agricultural drought transitions occurring over 20 and 60 days.

1. Introduction

Drought, which can last from weeks to decades, has tremendous socioeconomic and environmental impacts. The complex and seemingly chaotic nature of drought onset and decay has made accurate intraseasonal and subseasonal (2–4 week) drought prediction elusive. While strides have been made in the monitoring and understanding of drought over the past several decades, the broader atmospheric and hydrometeorological communities lack a strong dynamic understanding of how drought evolves on synoptic, subseasonal, and intraseasonal time scales, and in particular, what phenomena contribute to transitions toward or away from drought. The evolution of drought is complex and varies greatly depending on the time scales of interest.

Defined as a precipitation deficit over a given time period, drought can be divided into three categories based loosely on its duration: 1) *meteorological or climatological*, 2) *agricultural*, and 3) *hydrological drought* (Wilhite 2000; Dai 2011). The terminology is slightly ambiguous in that the three categories have overlapping definitions (Heim 2002; Dai 2011), making communication about the study and prediction of drought difficult.

Meteorological drought occurring during critical periods of the growing season is often characterized as agricultural drought. Agricultural drought (American Meteorological Society 2015), the focus of this study, usually occurs on time scales of 1–4 weeks or longer, and can have a direct impact on crop growth and yield. It is therefore also classified as *socioeconomic* drought, which is defined by the American Meteorological Society (AMS) as drought that affects the supply and demand of goods (https://www.ametsoc.org/ams/index.cfm/about-ams/ams-statements/statements-of-the-ams-in-force/drought/).

The onset of agricultural drought in the Great Plains often involves development of persistent, recurrent subsidence of air caused by large-scale atmospheric anticyclones, which lead to anomalously high surface temperatures via compression warming and lowered relative humidity (Namias 1955). Surface warming and lowered relative humidity over an extended period of time result in reduced soil moisture and evaporation promoting further surface warming, which can then

enhance the atmospheric anticyclonic circulation. While these anomalous atmospheric anticyclonic circulation patterns are often characterized by local feedbacks, they have also been shown to be associated with remote features, such as anomalous tropical sea surface temperatures (Giannini et al. 2003; Schubert et al. 2009; Cook et al. 2009).

SST in the tropical Pacific and North Atlantic Oceans (Piechota and Dracup 1996; Trenberth and Guillemot 1996; Ting and Wang 1997; Rajagopalan et al. 2000; Hoerling and Kumar 2003; Schubert et al. 2004a,b; Seager 2007; Seager et al. 2007, 2008; Schubert et al. 2008; Mo and Schemm 2008) can modify planetary wave patterns and storm tracks (Namias 1955; Schubert et al. 2004a, 2008), through modulation of deep convection and thermodynamic processes. Wu and Kinter (2009) concluded that Great Plains droughts (<3 months) have a statistically significant correlation with simultaneous SST in the tropical Pacific and subtropical North Atlantic Oceans, with a negative SST anomaly in the tropical Pacific and a positive SST anomaly in the North Atlantic Ocean corresponding to droughts. Wu and Kinter (2009) propose that SST forcing induces atmospheric circulation and precipitation anomalies, which affect soil moisture in the winter and spring and evaporation rates in the spring and summer, leading to summer droughts. However, the relationship between SST and atmospheric circulation anomalies does not occur in only one direction. Atmospheric circulation anomalies, such as the Madden–Julian oscillation (MJO; Zhang 2005) or atmospheric blocking, often influence the evolution of SST anomalies. These SST anomalies, especially those in the tropics, can then feed back on extratropical circulation anomalies (Lau 1997; Ding and Wang 2005; Frankignoul and Sennéchael 2007). Ultimately, all of these patterns can lead to variations in maize yields in the U.S. Corn Belt region (CBR).

The central plains drought of 2012 devastated crop yields throughout the CBR and impacted water storage and streamflow. During the spring, the 2012 drought lacked the low pressure systems that frequently bring rain to the region in normal years. The drought was further substantiated by the lack of afternoon convection during the summer. Hoerling et al. (2014) noted that the atmospheric circulation over the CBR during the summer of 2012 was characterized by considerable month-to-month variability. Precipitation was inhibited largely by zonal flow across the central plains in the spring, anticyclonic blocking over the central plains during June/July, and enhanced dynamical subsidence during August, as the CBR was located downstream of an anomalous ridge centered over the West Coast. This study led to the conclusion that the 2012 drought developed rapidly over the central Great Plains and was forced primarily by different types of natural variations in the weather at different stages of its lifetime. Hoerling et al. (2014) concluded that "variations neither in ocean states nor in greenhouse gases played significant roles in determining the intensity of the rainfall deficits in summer 2012" (p. 278).

Kumar et al. (2013) also studied the relationship between SST and soil moisture and the 2012 drought. Kumar et al. (2013) tested the hypothesis that extreme climate events, such as the 2012 drought, do not require extreme forcing. They suggest that the inability of numerical weather prediction to forecast extreme events, such as the 2012 drought, does not suggest biases in the models, but instead reflects a limit to predictability similar to that most notably described by Lorenz (1963), that is, stochastic weather events can lead to changes in climate states. Kumar et al. (2013), similar to Hoerling et al. (2014), concluded (via experiments with the Climate Forecast System v2 model) that the Great Plains drought of 2012 did not require extreme external forcing (e.g., SST anomalies) and could have arisen from atmospheric noise alone (e.g., weather events).

This study targets agricultural drought transition periods that occur over 20 and 60 days. These two durations were chosen to assess differences that might occur between the evolution of synoptic drought, and more persistent seasonal drought. Sensitivity analysis demonstrated that the 10- and 30-day transitions evolve similarly to 20-day transitions, and that 90-day transitions are similar to 60-day transitions. Atmospheric fields are filtered for low-frequency (periods >100 days), intraseasonal (periods between 20 and 100 days), and synoptic (periods <20 days) time scales, to compare the contributions to the evolution of drought transition periods by signals at these time scales, assessing the synoptic–dynamic processes leading to the onset or breakdown of agricultural drought. This study utilizes lag composites of basic atmospheric analysis fields as well as a diagnostic evaluation of the vertically integrated moisture budget across the continental United States and back trajectory analysis to better understand these transition periods.

2. Data

A CBR precipitation index is created from the NCEP Unified Gauge-Based Precipitation Dataset (UPD; NOAA/OAR/ESRL PSD 2016; Chen et al. 2008).This dataset contains a $0.25° \times 0.25°$ mesh of daily (1200–1200 UTC) precipitation observations over a 59-yr base period (1 January 1948–31 December 2006) for the region bounded by 20.125°–49.875°N, 230.125°–304.875°E. The UPD have been extended through the present, on a slightly shifted grid, and are updated daily.

TABLE 1. Number of events in each set of transition events.

	Drought decay	Drought onset
20 day	90	99
60 day	35	36

Various atmospheric fields are analyzed from the European Centre for Medium-Range Weather Forecasts interim reanalysis (ERA-Interim, hereafter ERA-I; Dee et. al. 2011; Berrisford et al. 2011). The ERA-I is used on its native Gaussian grid from 1979 to 2014. Specific humidity and zonal and meridional wind data are obtained at 27 vertical pressure levels, from 1000 to 100 hPa for diagnostic computation of the moisture budget over the United States. Since precipitation and evaporation are not analyzed fields in the model, F000–F024-h accumulated precipitation and evaporation initialized at 0000 UTC are obtained (ECMWF 2009). Geopotential height data at 200 hPa are used to analyze the circulation patterns commonly associated with CBR agricultural drought transition periods.

To analyze tropical convective anomalies concurrent with CBR agricultural drought transition periods, the National Oceanic and Atmospheric Administration outgoing longwave radiation (OLR) daily climate record is utilized (Lee 2014). Daily values of the OLR dataset are available from 1979 to the present on a $1.0° \times 1.0°$ global grid. For the purposes of this study, the OLR dataset is restricted from 30°N to 30°S and acquired from 1979 to 2014.

3. Methods

This study focuses on May–August. While maize yields are most sensitive to weather events occurring during pollination, which usually occurs during July, precipitation is relevant throughout the development of maize from seed germination to maturity (Huang et al. 2015). Therefore, any drought transition event that occurs throughout the growth stage is considered relevant to the development of the crop.

To identify transition events over the CBR, the UPD is averaged for grid points over Illinois, Indiana, Iowa, Minnesota, Missouri, Nebraska, Ohio, and South Dakota, creating a precipitation-based CBR index. Standardized CBR precipitation anomalies are computed by applying a power transformation to make the distribution of time series approximately symmetric, and then daily anomalies are created by removing the first five seasonal harmonics (1979–2014) from the time series. Anomalies are then normalized by the daily standard deviation. Agricultural drought transition periods are selected by creating a forward and backward looking

n-day accumulated standardized precipitation anomaly time series. Drought decay is defined as previous n-day accumulated precipitation anomalies ≤ -0.5 standard deviation followed by at least n-days of accumulated precipitation anomalies ≥ 0.5 standard deviations. Drought onset is the opposite scenario. This threshold was increased from -0.5 to -1.0 standard deviations and from 0.5 to 1.0 standard deviations and the results were similar, but with reduced sample sizes. Events are determined to be unique if there are $(n\text{-day})/2$ days between them. To demonstrate the different patterns associated with different time scales, n-day = 10, 30 days are investigated, equating to transitions occurring over 20 and 60 days. Hereafter, n-day = 10 will be referred to as 20-day drought onset or decay transition, whereas n-day = 30 is referred to as 60-day drought onset or decay transition. The minimum length drought in the 20-day transition events is 10 days, whereas the minimum length drought in the 60-day transition events is 30 days. There are 90 events in the 20-day drought decay transitions, 99 in the 20-day drought onset transitions, 35 in the 60-day drought decay transitions, and 36 in the 60-day drought onset transitions (Table 1). The mean increase in precipitation is approximately 26 mm for 20-day drought decay events and 42 mm for 60-day decay events, while the mean decrease in precipitation is 20 mm for 20-day onset events and 37 mm for 60-day onset events. For all transition types, the events tend to be evenly distributed throughout May–August. There is also a 40% increase in the number of drought onset events between 1979–88 and 2006–15.

A census of the anomaly correlation of events to the composite mean is calculated to determine the similarity of events to the composite mean. This is done by computing anomaly correlations between the data fields of each event and the composite mean at each lag (from 10 days prior to the transition to 10 days after). The average anomaly correlation is then taken across the lags and events. Events with a positive anomaly correlation are considered to evolve similarly, while events with a negative anomaly correlation are considered to evolve differently.

Back trajectories are calculated using the NOAA Hybrid Single-Particle Lagrangian Integrated Trajectory model (HYSPLIT; Stein et al. 2015) to determine the source locations of parcels over the CBR during drought transition periods. For each transition type, back trajectories are initialized at 50 and 1500 m and are calculated to 168 h prior to the transition day. One trajectory is released at each level, from each of 10 grid points spaced throughout the CBR, yielding 20 trajectories calculated for each event. A k-means clustering algorithm based on Euclidean distance is then used to

Lagged Composites of 20-Day Drought Transitions
a. 20-Day Drought Decay | Lag: -10

b. 20-Day Drought Decay | Lag: 0
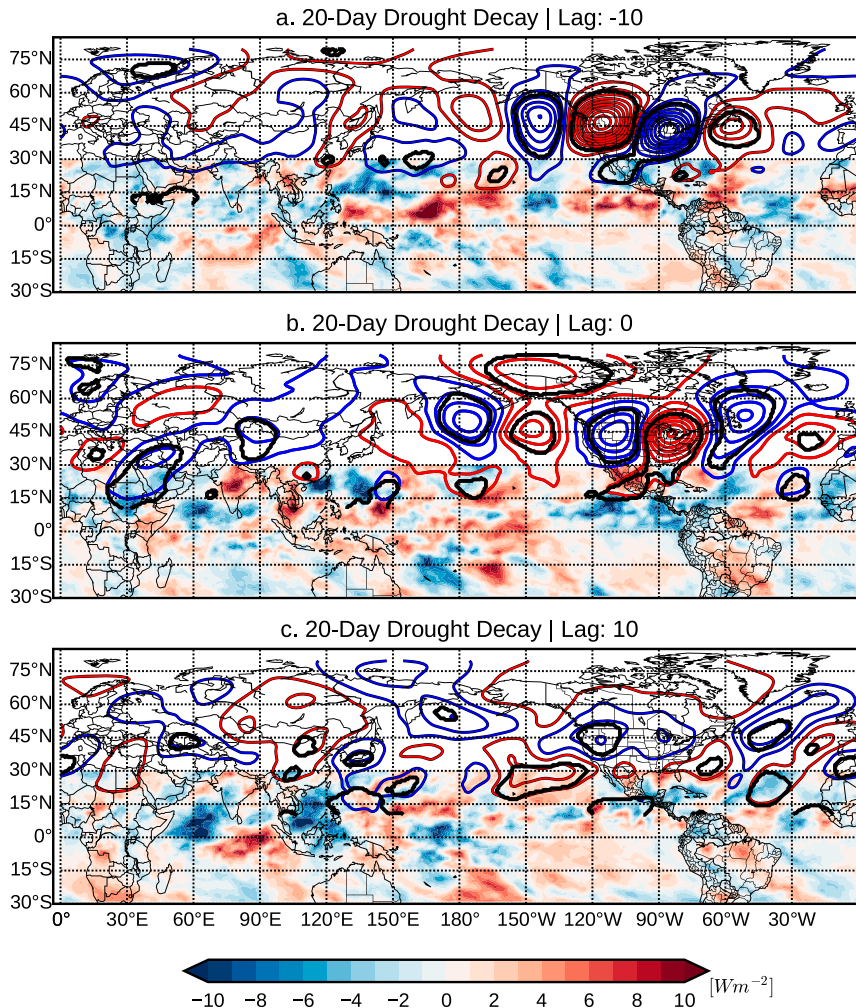

c. 20-Day Drought Decay | Lag: 10

FIG. 1. Composite 200-hPa geopotential height anomalies contoured every 10 m, starting at ± 5 m, and OLR anomalies (shaded) for (a)–(c) 20-day drought decay and (d)–(f) 20-day drought onset transition. The composite mean patterns (a),(d) 10 days before the transition; (b),(e) at the transition day; and (c),(f) 10 days after the transition. The solid black line indicates where 200-hPa anomalies are statistically different from zero at the 95th percentile level. OLR anomalies tend to become significant at ± 2 W m^{-2}.

identify similar source regions of parcels based on the parcel locations 168 h before the set of all drought onset and decay transition events. The k-means approach is iterative, and aims to find an optimal number of n clusters such that members within a cluster are close to each other, but far from other clusters. Riddle et al. (2013) provide a detailed discussion on k-means clustering and its benefits and drawbacks. Here, the clusters are trained on normalized latitude, longitude, and level. Unlike Riddle et al. (2013), the silhouette value is used here to determine the optimal number of clusters.

The silhouette approach to determining the optimal number of clusters is primarily a graphical analysis that

demonstrates how similar points inside a cluster are to each other and to other clusters (Rousseeuw 1987). A mean silhouette value of one is the optimal solution, while mean silhouette values of zero indicate the clusters are poorly chosen. Clusters are computed iteratively from 2 to 10, and the local maximum in mean silhouette value is chosen as the appropriate number of clusters. In this case, five clusters reach the local maximum in mean silhouette value (0.48). These five clusters are used to understand how parcels of moist and dry air are transported into the CBR during transition events, and to identify the parcel source regions. The 925–850-hPa-averaged gridpoint specific humidity at time = 0 is used

Lagged Composites of 20-Day Drought Transitions

d. 20-Day Drought Onset | Lag: -10

e. 20-Day Drought Onset | Lag: 0
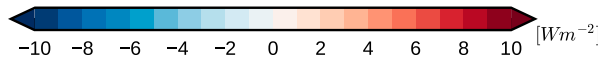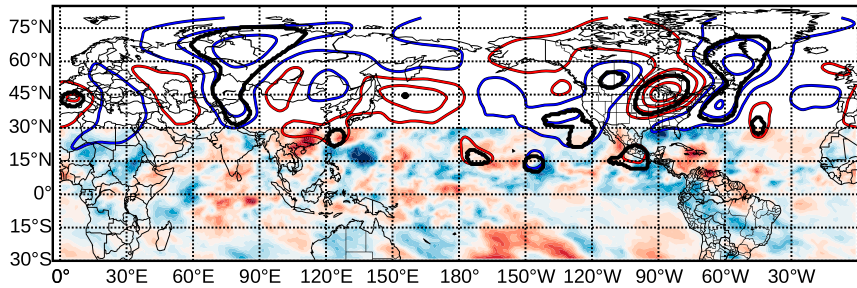
f. 20-Day Drought Onset | Lag: 10

$[Wm^{-2}]$
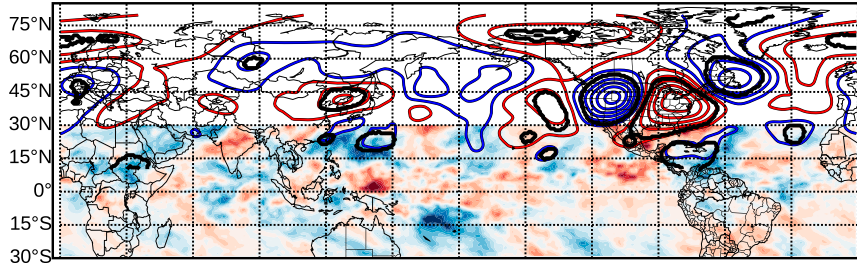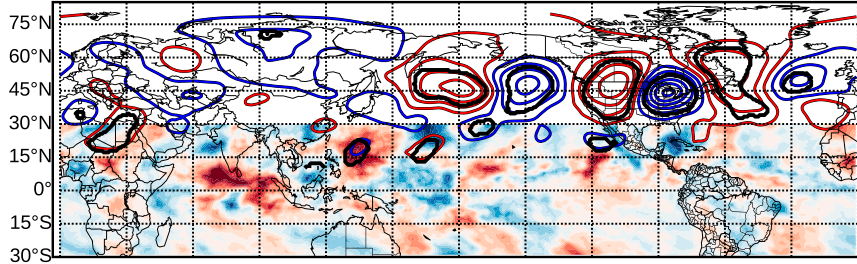
FIG. 1. (*Continued*)

to compute the relative contribution of low-level moisture each trajectory has to the transition event, which is presented in section 5.

Composites of the vertically integrated moisture budget are then computed for both the drought onset and decay transitions:

$$P - E = -\frac{\partial}{\partial t}\left(\frac{1}{g\rho_w}\int_{p_s}^{p_t} q\, dp\right) - \frac{1}{g\rho_w}\int_{p_s}^{p_t} \mathbf{V} \cdot \nabla q\, dp$$
$$- \frac{1}{g\rho_w}\int_{p_s}^{p_t} q\nabla \cdot \mathbf{V}\, dp - \frac{1}{g\rho_w}q_s\mathbf{V}_s \cdot \nabla p_s + R, \quad (1)$$

where P is the precipitation, E is the evaporation, p_s is the surface pressure, p_t is the upper bound (100 hPa), g is the acceleration due to gravity, ρ_w is the density of water, q is the specific humidity, $\mathbf{V}$ is the horizontal velocity vector, q_s is the 2-m specific humidity, $\mathbf{V}_s$ is the 10-m horizontal

wind vector, and R is the budget residual. Seager and Henderson (2013) found that diagnosed moisture budgets computed in a similar fashion can be reasonably examined to determine the causes of hydroclimate anomalies, even though precipitation − evaporation cannot be balanced in the long-term mean.

Similar to Sakaeda and Roundy (2015), temporal linear decomposition of the moisture budget is used to examine the dynamical processes that contribute to drought transition periods. The horizontal wind and specific humidity are decomposed into three temporal bands, as follows:

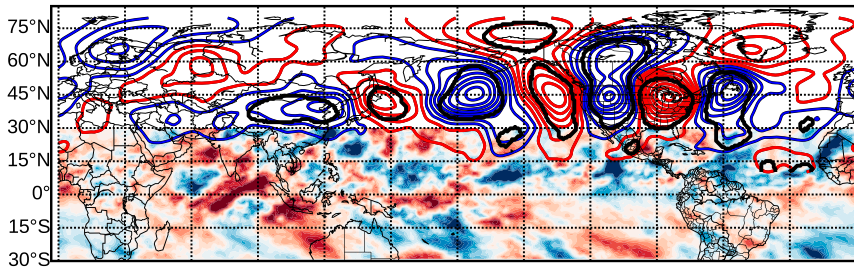$$\mathbf{V} = \overline{\mathbf{V}} + \mathbf{V}^* + \mathbf{V}';\, q = \overline{q} + q^* + q',$$

where the overbar indicates the low-frequency time scale with periods >100 days, the asterisk indicates the intraseasonal time scales with periods of 20–100 days,

Lagged Composites of 20-Day Drought Transitions

a. 60-Day Drought Decay | Lag: -10
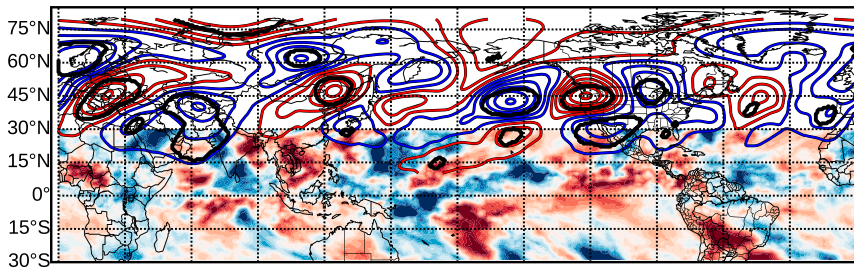
b. 60-Day Drought Decay | Lag: 0

c. 60-Day Drought Decay | Lag: 10

$[Wm^{-2}]$
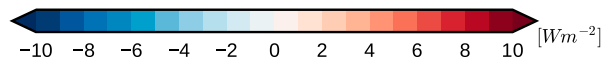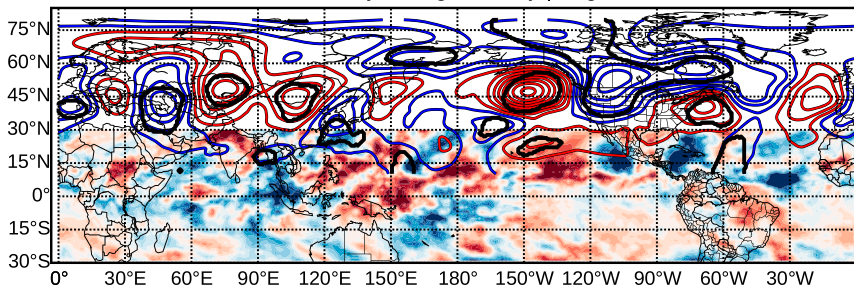
−10 −8 −6 −4 −2   0   2   4   6   8   10

FIG. 2. As in Fig. 1, but for 60-day drought transition.

and the prime indicates the synoptic, including time scales shorter than 20 days. Each term is expanded accordingly and its amplitudes analyzed. Any term that accumulates less than 2 mm over the 10 days leading up to or after a transition is considered insignificant and is not presented.

A Monte Carlo test is applied to the data to test for statistical significance. Events from the population of each composite are drawn at random 1000 times with replacement to generate 1000 new composites. The data from the new composites are then tested for statistically different signals from zero at the 95th percentile.

4. Atmospheric evolution

Composite mean 200-hPa geopotential and OLR anomalies are presented for 20- and 60-day drought onset and decay. The composite unfiltered anomalies for

20- (Fig. 1) and 60-day (Fig. 2) drought transitions are presented for reference. Wavenumber–frequency spectrum analysis of the composite mean 200-hPa geopotential anomalies reveals that standing oscillations and propagating patterns dominate the intraseasonal band, with emphasis on eastward propagation (not shown), while eastward-propagating patterns dominate the synoptic scales and stationary waves dominate the low-frequency components (spectra not shown). Section 4a describes the low-frequency patterns associated with 20- and 60-day decay and onset transitions, while section 4b discusses the intraseasonal and synoptic patterns.
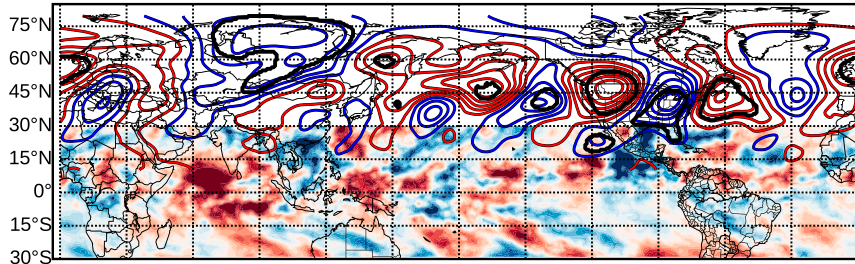
a. Low-frequency patterns

The low-frequency base states for 60- and 20-day agricultural drought onset and decay are remarkably similar over the Western Hemisphere, and are

Lagged Composites of 60-Day Drought Transitions

d. 60-Day Drought Onset | Lag: -10
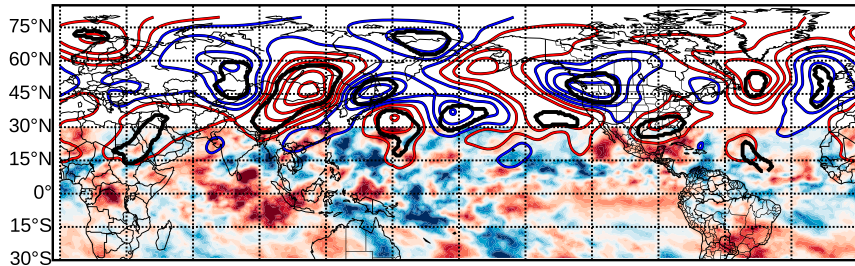
e. 60-Day Drought Onset | Lag: 0
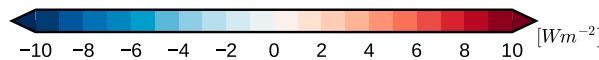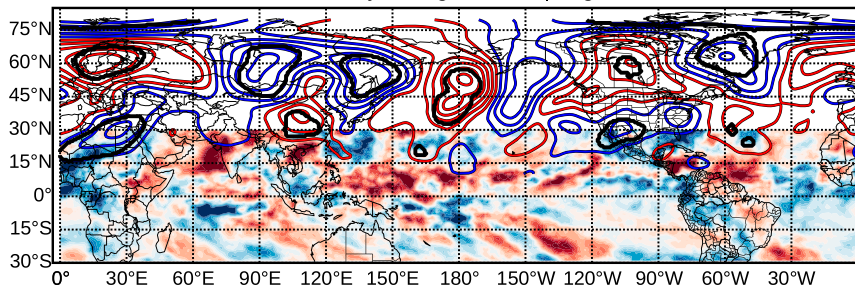

f. 60-Day Drought Onset | Lag: 10

FIG. 2. (*Continued*)

characterized by a stationary wave. A two tailed Student's *t* test reveals that the two populations are statistically similar across the Northern Hemisphere (not shown). Both 20-day drought onset and decay transitions are characterized by an anomalous low-frequency ridge over Alaska, which is statistically different from zero in the decay cases, as well as an anomalous low-frequency ridge over the southeastern United States, which is statistically different from zero in the onset cases (Fig. 3). This low-frequency pattern favors a trough over the western half of the United States, allowing for anomalous low-frequency moisture transport toward the CBR and cyclone development, but the Alaska ridge can favor southward flow into the CBR, which can favor dry air. The 60-day drought onset transition favors a weak ridge anomaly across the CBR and western United States (Fig. 3d). Interestingly, the largest differences between the two

low-frequency base states occur over Eurasia and the Pacific Ocean.

In both the 20- and 60-day drought decay transitions, an anomalous trough is displaced equatorward from the anomalous Alaskan ridge and anomalous troughs are centered over eastern Russia and China (Figs. 3a,b). During drought onset, the anomalous ridge over China is more amplified, and there is no anomalous trough present in the Gulf of Alaska (Figs. 3c,d). Both the drought decay and onset transitions favor wave breaking associated with the ridge over Alaska. Through anticyclonic wave breaking, a trough is injected into the tropics, aiding in the organization of convection over the eastern Pacific Ocean (Matthews and Kiladis 1999; MacRitchie and Roundy 2016).

The similarity over North America between the low-frequency patterns toward or away from drought suggests that this background pattern might be conducive to

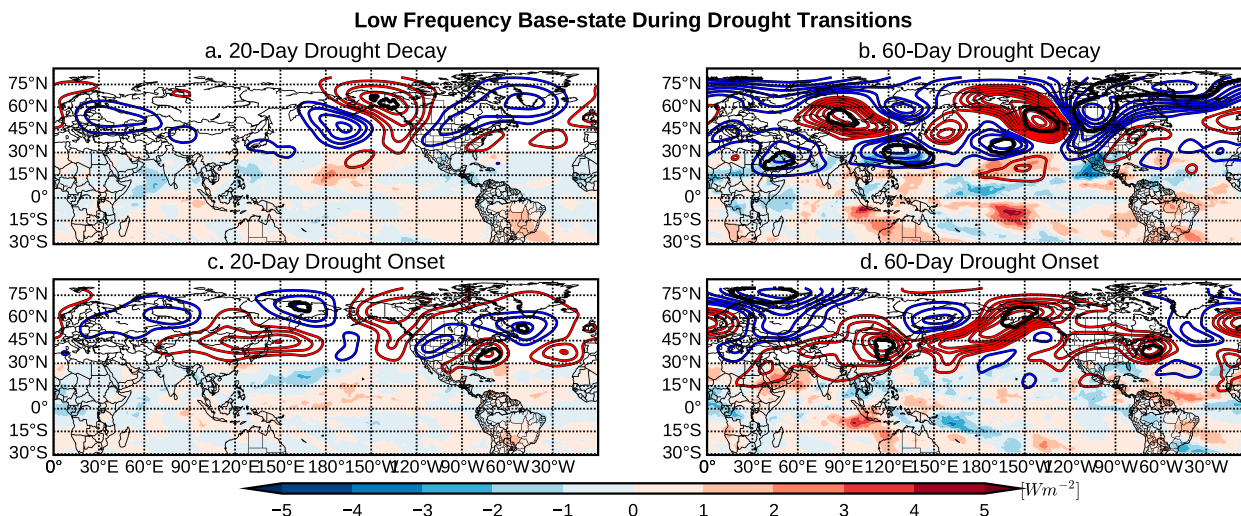**Low Frequency Base-state During Drought Transitions**

FIG. 3. Composite low-frequency 200-hPa geopotential height anomalies contoured every 2 m and OLR anomalies (shaded) for (a) 20-day drought decay, (b) 60-day drought decay, (c) 20-day drought onset, and (d) 60-day drought onset transition. The solid black line indicates where 200-hPa anomalies are statistically different from zero at the 95th percentile level. OLR anomalies tend to become significant at $\pm 1\,\mathrm{W\,m^{-2}}$.

strong fluctuations between moist and dry, possibly because small shifts in the pattern could yield transitions in the dominance of flow from the northwest versus off the Gulf of Mexico. This hypothesis is tested by projecting daily low-frequency 200-hPa geopotential anomalies onto the composite mean low-frequency 200-hPa geopotential anomalies over the Western Hemisphere to create a time series of the amplitude of the projection onto the composite mean pattern. This time series is then normalized by its seasonal standard deviation. The number of times a 20-day onset or decay transition occurs is tallied for when the projection time series is $>1.0\sigma$, $<-1.0\sigma$, or in between. These values are then normalized by the total number of days the climatology (May–August) spends in each bin. The results demonstrate that a 20-day drought transition in either direction is nearly twice as likely to occur during strong projections onto the composite mean low-frequency state (5.95%), compared to the opposite pattern (3.23%), and 1.5 times more likely to occur than for conditions in between the two extremes (4.11%).

While the geopotential patterns are similar, the low-frequency tropical convection patterns show contrast between the drought onset and decay transitions (Fig. 3). The 20-day drought decay transitions favor suppressed low-frequency convection centered on 15°N near 180°, while the 20-day drought onset transitions favor active convection in this region (Figs. 3a,c). These differences are statistically significant at the 95% level and amplitudes are stronger in the 60-day composites. The 60-day drought decay transitions show active convection on the equator from 150°E to 135°W (Fig. 3b).

Diabatic heating associated with this convection builds an anomalous ridge poleward in both hemispheres, favoring the Rossby wave train in the Northern Hemisphere in both the 20- and 60-day drought decay transition composites (Figs. 1 and 2). Low-frequency convection in this region is absent in the drought onset composites, which are characterized by different extratropical wave patterns (Figs. 3c,d). The low-frequency patterns do not change significantly ±20 days from the transition day, indicating that although drought onset and decay occur in slightly different low-frequency base states, the transitions are not preceded by shifts in the low-frequency base states (not shown).

b. Intraseasonal and synoptic patterns

The largest differences leading up to and following the transitions toward or away from drought occur in the intraseasonal band. Both the 20- and 60-day drought onset and decay favor amplification of an anomalous Rossby wave train over the United States (Figs. 1 and 2). The composite 20-day transition away from drought indicates an intraseasonal wave train 10 days before drought breakdown, featuring an anomalous ridge/trough pattern over the western and eastern half of the United States, downstream of an anomalous trough in the Gulf of Alaska and a ridge over the north-central Pacific Ocean (Fig. 4a). This intraseasonal wave train is relatively stationary from 15 to 5 days prior to drought breakdown (not shown), before propagating eastward by the transition day (Fig. 4b). This period of rapid propagation corresponds to swapping between two opposite states of the standing wave. The eastward propagation breaks down the
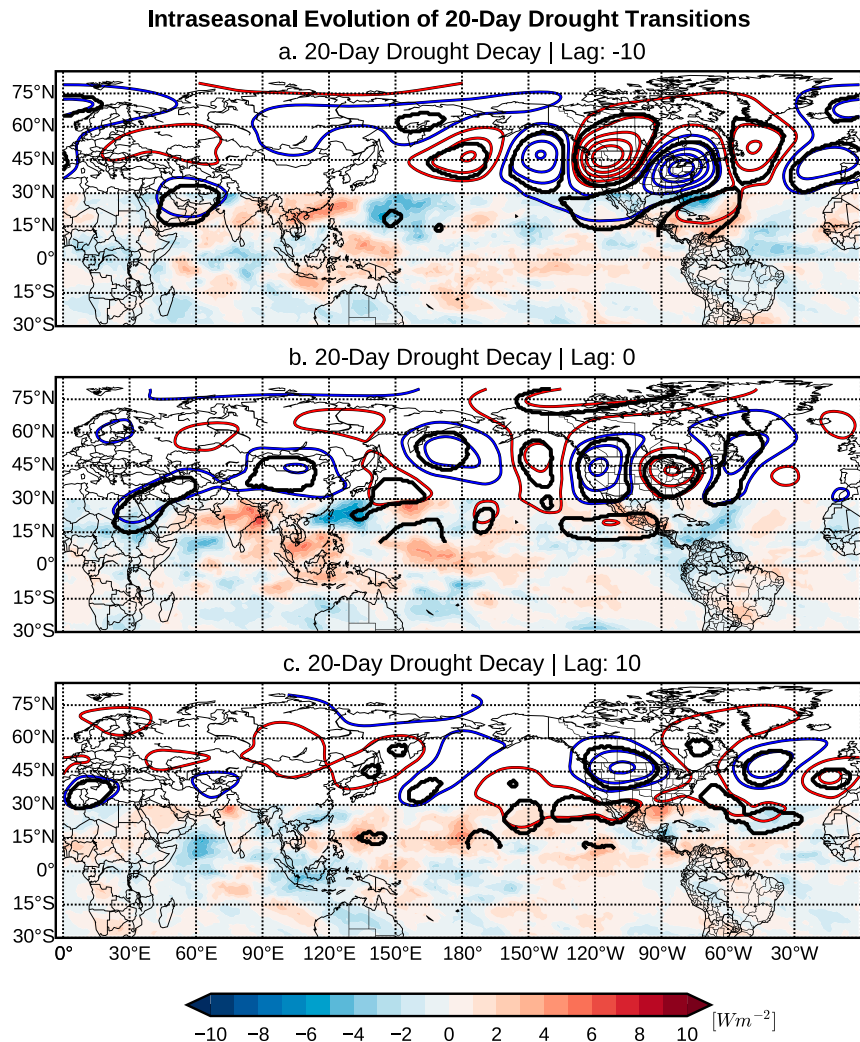
Intraseasonal Evolution of 20-Day Drought Transitions

FIG. 4. Composite intraseasonal 200-hPa geopotential height anomalies contoured every 10 m, starting at ±5 m, and OLR anomalies (shaded) for 20-day drought (a)–(c) decay and (d)–(f) onset transition. (a),(d) At 10 days prior to the transition; (b),(e) on the transition day; and (c),(f) 10 days after the transition. The solid black line indicates where 200-hPa anomalies are statistically different from zero at the 95th percentile level. OLR anomalies tend to become significant at ±1 W m^{-2}.

anomalous ridge over the central plains and develops an anomalous trough over the West Coast, with an anomalous ridge over the East Coast of the United States (Fig. 4b). Together, these circulation anomalies support anomalous southerly flow off the Gulf of Mexico, bringing moisture to the CBR. Further, the CBR is downstream of an anomalous trough, bringing dynamic support for widespread ascent and cyclone or mesoscale convective system development, allowing for rain over the CBR. The 60-day transition away from drought evolves similarly on intraseasonal time scales (Fig. 5).

The intraseasonal evolution of transitions toward drought is much different. For 20-day drought onset,

the zonal extent of the anomalous wave train is much narrower than during drought decay (Fig. 4d). An anomalous intraseasonal trough over the CBR, flanked by anomalous ridging to its east and west persists from 15 to 5 days prior to drought onset. This wave quickly propagates eastward, developing a stationary ridge over the CBR, which persists for 10 days after the transition (Fig. 4f). The 60-day drought onset shows a similar intraseasonal wave progression; however, the drought conditions persist for 20–30 days after the transition (not shown). Drought transition events of either sign or duration occur at roughly twice the climatological rate when the observed pattern projects
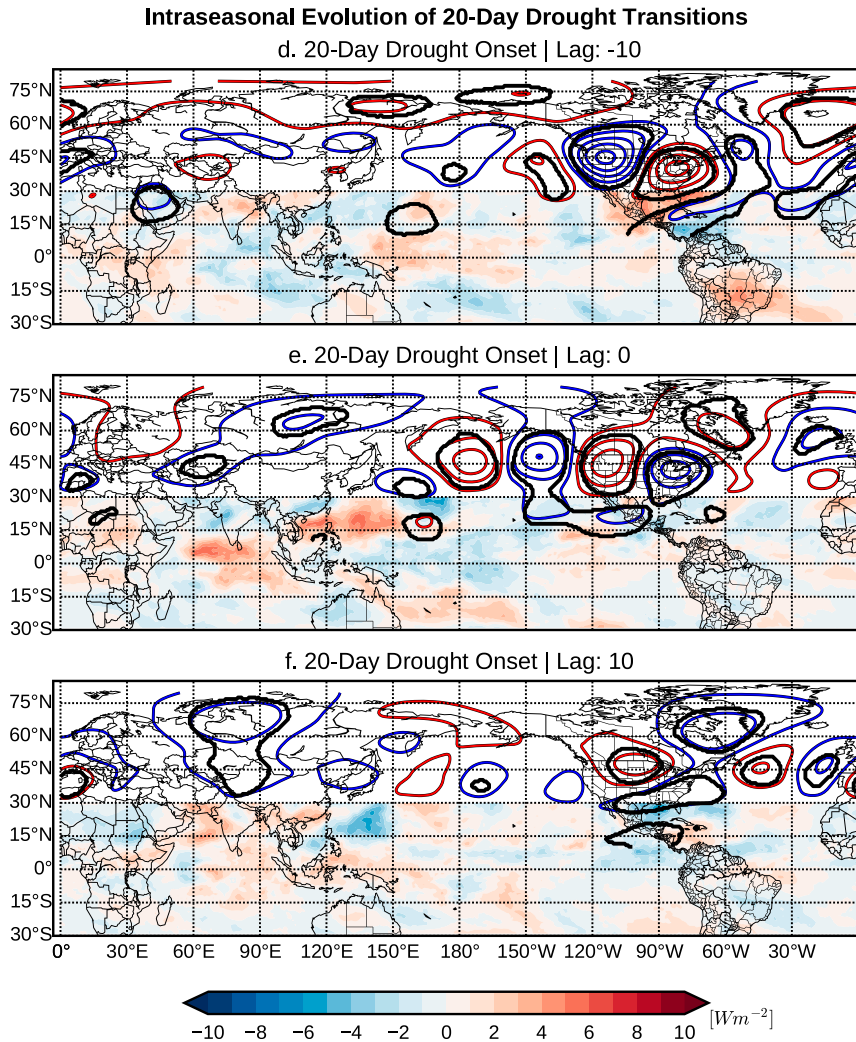
Intraseasonal Evolution of 20-Day Drought Transitions

d. 20-Day Drought Onset | Lag: -10

e. 20-Day Drought Onset | Lag: 0

f. 20-Day Drought Onset | Lag: 10

FIG. 4. (*Continued*)

positively onto the composite mean pattern for the same sign (not shown).

The intraseasonal OLR anomalies for the 20-day drought transitions are generally weak, but do show some differences (Fig. 4). At 10 days prior to the 20-day drought decay, there is a composite minimum in intraseasonal OLR between 15° and 30°N centered at 135°E (Fig. 4a). Conversely, a maximum in OLR is present over this region during 20-day drought onset (Fig. 4d). By drought decay, the intraseasonal convective maximum shifts westward (Fig. 4b), which is also evident in the total OLR anomaly field (Fig. 1b). This slowly evolving westward-propagating wave is apparent when plotted in the longitude–time domain (Fig. 6a). The amplification of the extratropical Rossby wave is coincident with flare-ups in the OLR anomalies associated with this westward-moving wave 15 days and 2 days

prior to drought decay, with each flare-up followed by a shift in the phase of the extratropical Rossby wave (Fig. 6a). The census of the events, computed from intraseasonal OLR data averaged from 15° to 30°N, shows that 64% of the 20-day events evolve similarly to the composite. However, even a composite generated from the remaining 36% events that evolve differently contains this westward-propagating feature (Fig. 7b). The OLR anomaly pattern is shifted roughly 180° out of phase during the 20-day drought onset from the pattern during the 20-day drought decay and this phase shift is also tied to a 180° shift in the phase of the extratropical Rossby wave (Fig. 6c). A similar census determined that 90% of the 20-day drought onset events evolved similarly, and the remaining 10% of events also demonstrate the phase-shifted westward-propagating wave (Figs. 7c, d). Extratropical waves intrude (via anticyclonic wave
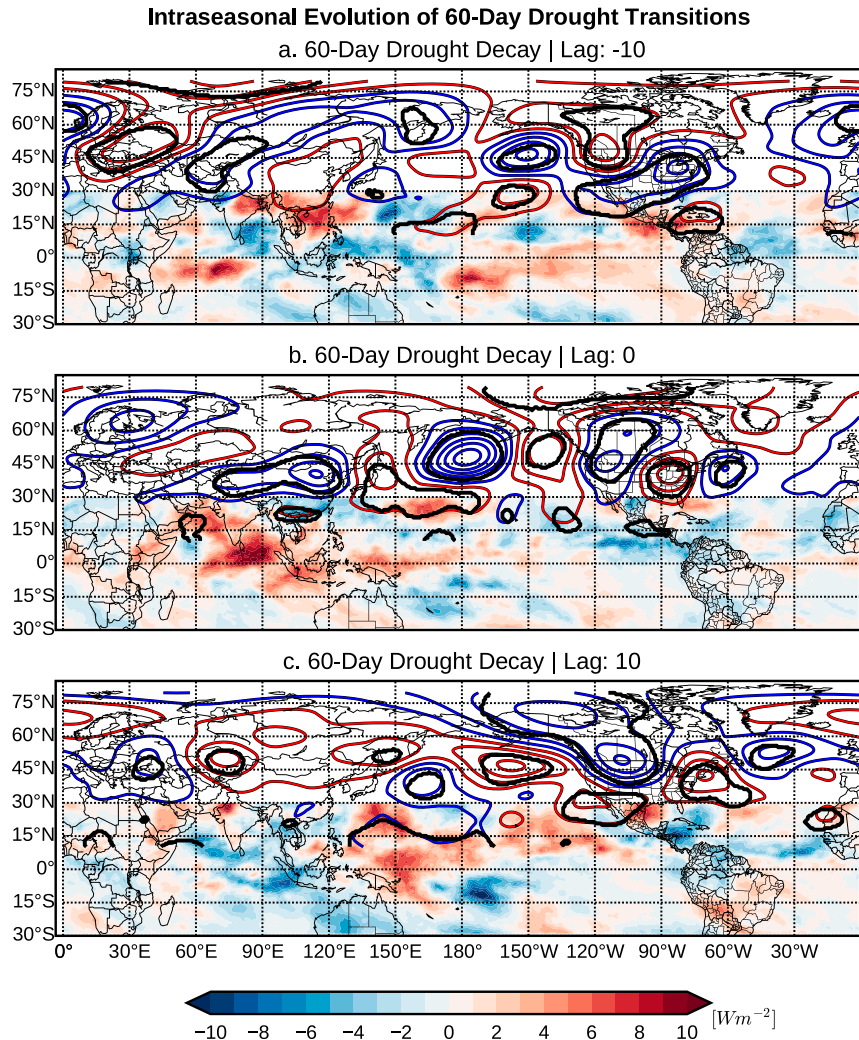
Intraseasonal Evolution of 60-Day Drought Transitions

FIG. 5. As in Fig. 4, but for 60-day drought transition. OLR anomalies tend to become significant at $\pm 2\,\mathrm{W\,m^{-2}}$.

breaking) into the tropics and organize convection, which then feeds back into the extratropical circulation (not shown). This process is well documented and occurs frequently over the Pacific Ocean and Maritime Continent (Matthews and Kiladis 1999; MacRitchie and Roundy 2016; Sakaeda and Roundy 2015; Gloeckler and Roundy 2013).

The 60-day drought transitions are characterized by much different intraseasonal OLR patterns than the 20-day intraseasonal composites. The anomalous westward-propagating convection present from 15° to 30°N in the 20-day drought decay transition is not as prevalent (Fig. 6b). Instead, there is an eastward-propagating signal of active convection on the equator (averaged 10°N–10°S) that takes roughly 40 days to circumnavigate the globe (Fig. 8a). In the 60-day drought onset composites, the eastward-propagating

wave is in phase with the 60-day decay composites (Figs. 8b,d), making it difficult to use such a signal as an identifier for drought transition. The largest differences between the OLR anomalies during the 60-day drought onset and decay are in their phase speeds and amplitudes. That is, the 60-day drought onset transition is characterized by a much slower and weaker eastward-propagating signal than the positive transition (Figs. 7b,d). There has been little research into the differences between fast and slow intraseasonal convective events, so this finding encourages further study.

While important, the synoptic evolution of these signals is noisy. At 10 days prior, at the transition, and 10 days after each transition type, the synoptic patterns are largely in phase with the intraseasonal patterns, although they are much weaker (not shown), and are mostly eastward propagating. Since synoptic variability
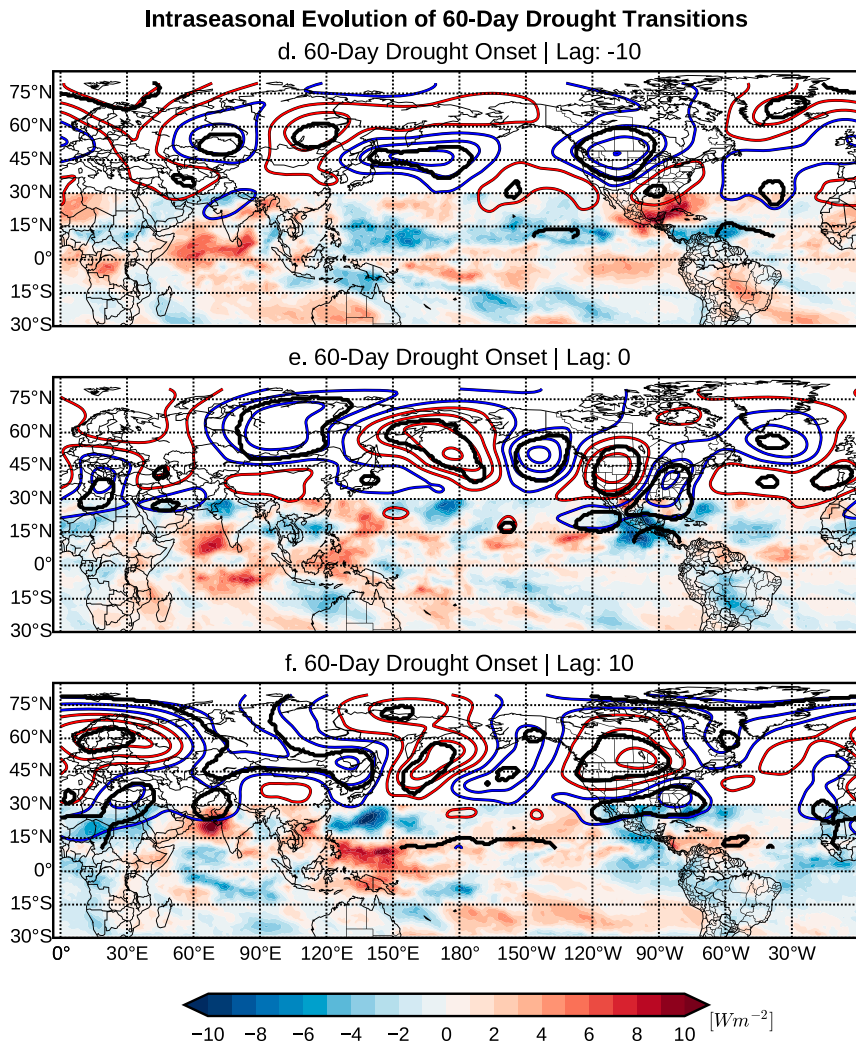
Intraseasonal Evolution of 60-Day Drought Transitions

d. 60-Day Drought Onset | Lag: -10

e. 60-Day Drought Onset | Lag: 0

f. 60-Day Drought Onset | Lag: 10

FIG. 5. (*Continued*)

in midlatitude geopotential height anomalies is typically stronger than intraseasonal variability, this result suggests substantial variation across the set of events. Together, the synoptic and intraseasonal patterns explain most of the signal in the total composites (not shown), and therefore have the largest contributions to drought transition periods.

5. Source regions of air parcels

Understanding where air parcels originate and the pathways they tend to follow prior to agricultural drought transitions over the CBR is critical for understanding how moisture (or dry air) gets transported into the region during agricultural drought transitions. Cluster analysis determines that there are five main source regions for parcels entering the CBR during

drought transition periods (Fig. 9). These source regions are from the eastern half the United States and the Gulf of Mexico (cluster 0), off of the West Coast of the United States (cluster 1), over Canada (cluster 2), in the central Pacific basin (cluster 3), and over Eurasia/ western Pacific Ocean (cluster 4; Fig. 9). The cluster analysis determines that parcels originate in both 20-day drought onset and decay transitions from each of these areas, but the number of parcels in each cluster changes for each category type (Table 2). These source regions are representative of the 60-day transitions. However, there are noticeably more parcels originating over the Caribbean/Gulf of Mexico in the 60-day decay events, with a lack of parcels originating in these regions during the 60-day onset events. There are nearly twice as many trajectories originating in cluster 0 in transitions away from drought than toward drought, while there are 1.5–2
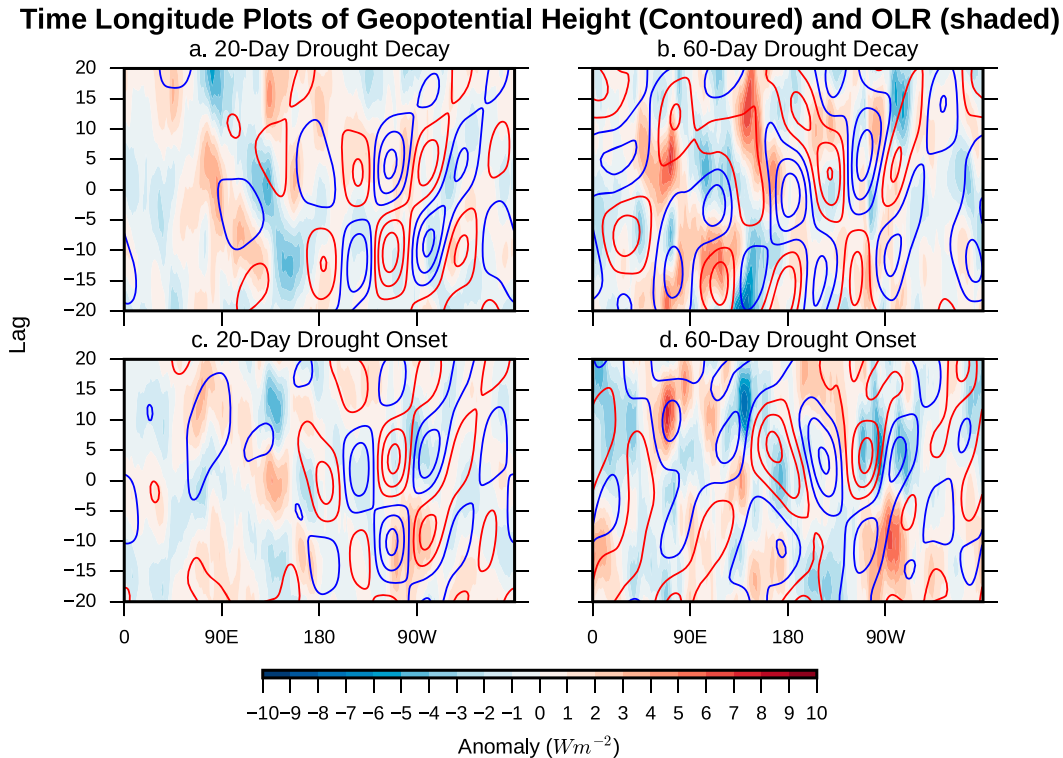
Time Longitude Plots of Geopotential Height (Contoured) and OLR (shaded)

FIG. 6. Time–longitude diagrams of (left) 20- and (right) 60-day (a),(b) decay and (c),(d) onset. Shaded contours are OLR anomalies averaged 15°–30°N, blue dashed contours are 30°–60°N averaged negative 200-hPa geopotential anomalies, and red solid contours are 30°–60°N averaged positive 200-hPa geopotential anomalies. Geopotential anomalies are contoured every 10 m, starting at ±5 m. OLR anomalies tend to become significant at ±2 W m^{-2}.

times as many trajectories in clusters 1, 2, and 4 in transitions toward drought compared to transitions away from drought. Trajectories coming off of the Gulf of Mexico would contribute to the largest net moistening in the lower levels, while parcels sourced from the other regions tend to be drier.

The local low-level moisture impact associated with each trajectory in each cluster demonstrates differences in local moisture impact between 20-day drought onset and decay. In the net, both 20-day drought onset and decay transitions have more relatively dry parcels than relatively moist parcels (Fig. 10a). Since we are only sampling a relatively small fraction of the variance of moisture transport into the region for each event in each transition, this result is not surprising. The drought onset transitions are characterized by a roughly 70/30 split of dry to moist parcels, while the drought decay transitions feature a 55/45 split (Fig. 10a). In nearly every cluster (except cluster 1, which is dominated mostly by upper-level parcels), the drought decay transitions have a smaller ratio of wet to dry parcels than the drought onset transitions. This result means that the moisture characteristics of parcels originating from these

regions are different between during drought onset and decay.

For both types of transition events, parcels that originate off of the Gulf of Mexico and over the central United States have a smaller dry-to-wet ratio than the other clusters (Fig. 10b). Both drought decay and onset transition events have trajectories originating from this region; however, 65% of the total number of trajectories in this cluster is from drought decay events (Fig. 11). This difference leads to a larger amount of moisture originating from the Gulf of Mexico during drought decay, which is not surprising given the synoptic evolution of these events (Fig. 1). Interestingly, cluster 4, or parcels that originated over the central Pacific, shows the largest differences in dry-to-wet ratio between drought onset and decay (Fig. 10f). These differences can be attributed to more parcels subsiding and drying during drought onset (Fig. 12). Further, this cluster contains 30% more trajectories from drought onset events, implying more subsidence during drought onset (Fig. 12). This result highlights that although parcels during drought onset and decay originate in the same source regions, the different transition types prefer
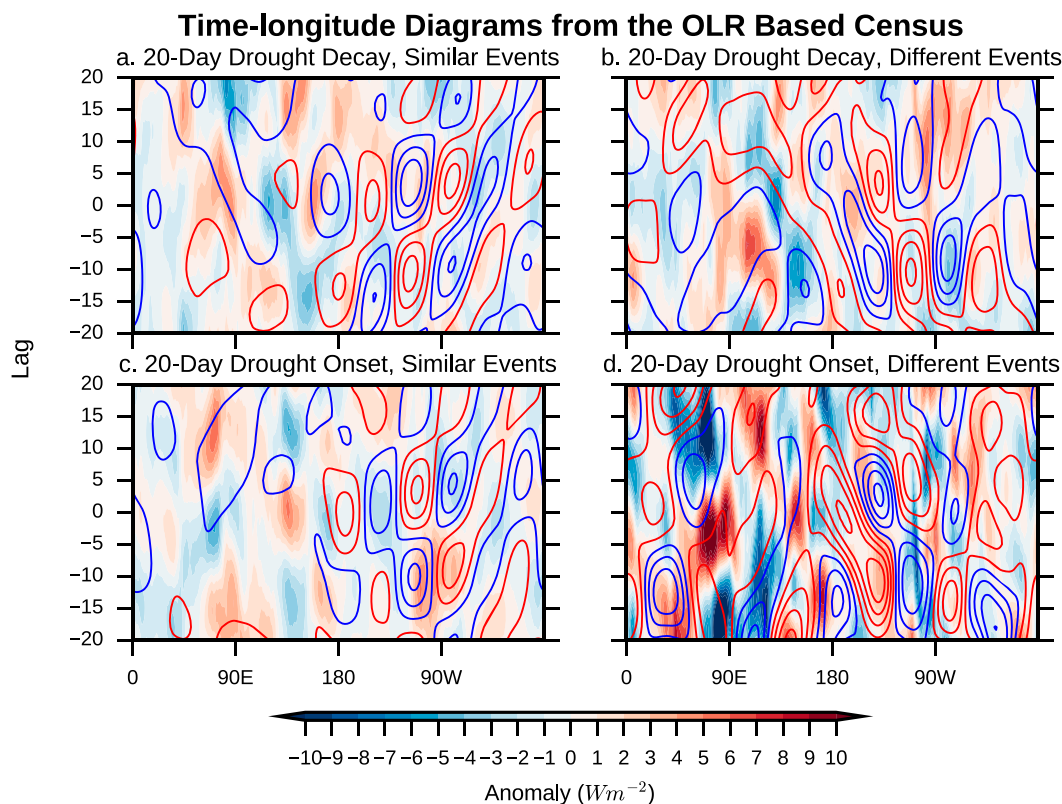
Time-longitude Diagrams from the OLR Based Census

FIG. 7. Time–longitude diagrams of 20-day drought onset and decay transition events that evolve (a),(c) similarly to and (b),(d) different from the composite mean OLR averaged 15°–30°N. Blue dashed contours are 30°–60°N averaged negative 200-hPa geopotential anomalies, and red solid contours are 30°–60°N averaged positive 200-hPa geopotential anomalies. Geopotential anomalies are contoured every 10 m, starting at ±5 m. OLR anomalies tend to become significant at ±2 W m^{-2}.

different clusters and parcels originating from these clusters have different moisture characteristics that result from their different vertical pathways to the CBR. While only 20-day transition events have been analyzed here, the results are similar for 60-day transition events.

6. Moisture budget

Understanding the time scales of moisture transport, as well as parcel locations, into the CBR during drought transition periods is also critical for understanding how these events evolve. The boundary term is important only in regions where elevation changes rapidly, and is not discussed. As demonstrated by Seager and Henderson (2013), the budget cannot be closed and the residual is large. Since the results are focused on the relative magnitudes of the linearly decomposed advection and convergence terms, the residual is not discussed. While this section focuses mainly on the 20-day transition events, the results are similar for 60-day transition events.

Accumulated moisture advection over the CBR from 10 days prior to 20-day drought decay, to the transition day, is positive over much of the region (Fig. 13). Although the moisture advection is positive, the moisture convergence during this period is negative. This means that, while there is moisture being advected into the CBR, there is no precipitation. After the transition occurs, a regime shift supports moisture convergence and rain (Fig. 1). The opposite scenario is true during drought onset.

The dominant term in the advection of moisture over the CBR during 20-day drought onset and decay is the advection of low-frequency moisture by the low-frequency wind (Fig. 14). This result is not surprising, as the low-frequency moisture gradient strengthens in the summer. Thus, changes in low-frequency moisture transport are not the primary forcing mechanisms for drought onset and decay. The largest differences between drought onset and decay events occur in the other terms. The term with the largest net change across the transition period, and largest difference between the transitions, is the advection of intraseasonal moisture by the intraseasonal wind.

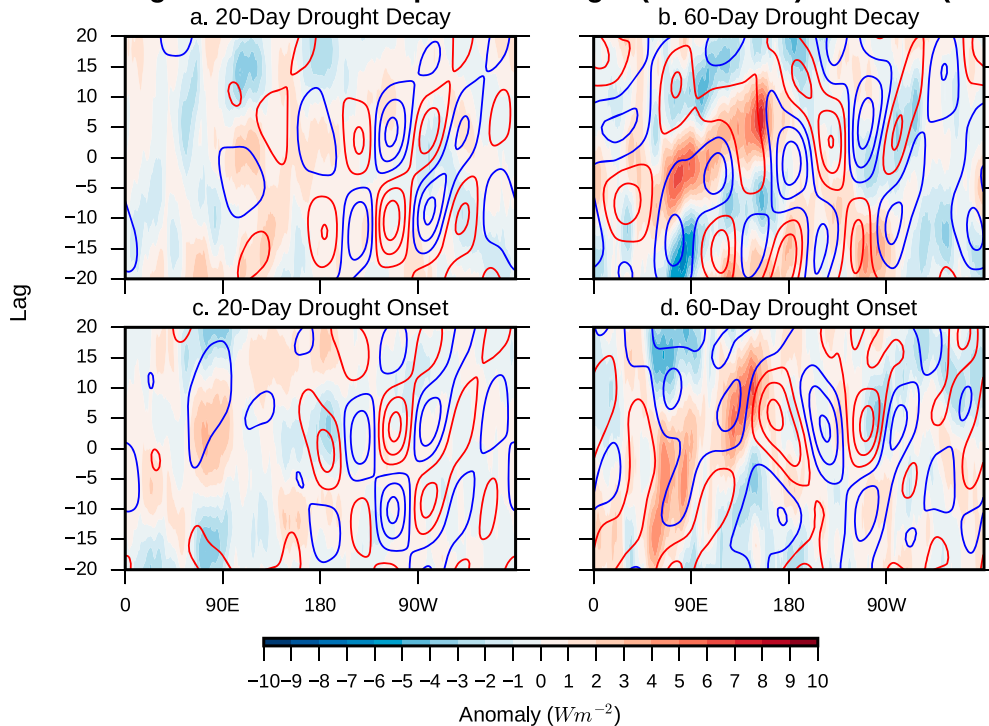## Time Longitude Plots of Geopotential Height (Contoured) and OLR (shaded)

FIG. 8. As in Fig. 6, but OLR anomalies are averaged from 10°N to 10°S.

During drought decay, the advection of intraseasonal moisture by the intraseasonal wind reaches a minimum 10 days prior to the transition event before rapidly increasing to a maximum after the transition (Fig. 14a). This increase coincides with an increase in the total

advection, from negative to positive values. Two other terms that contribute significantly to the total increase in moisture advection are the advection of intraseasonal moisture by the low-frequency wind and the advection of synoptic moisture by the low-frequency wind.
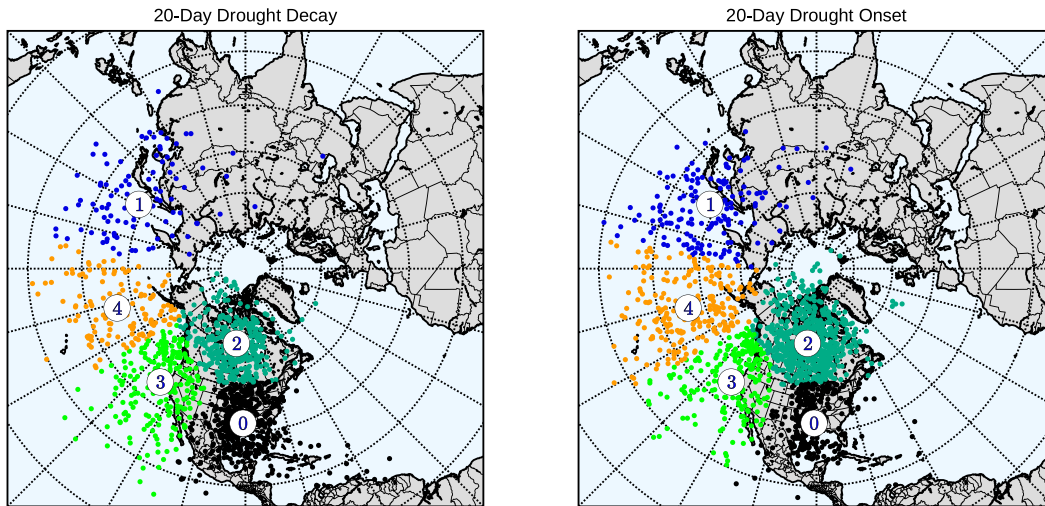
Cluster locations

FIG. 9. Locations of each trajectory at $t = -168$ h in their respective clusters sorted by 20-day drought (left) decay and (right) onset transition periods.

TABLE 2. Number of trajectories in each cluster, for decay and onset transition events.

	Decay	Onset
Cluster 0 (Gulf of Mexico/eastern United States)	507	279
Cluster 1 (Canada)	99	150
Cluster 2 (east Pacific/western United States)	391	661
Cluster 3 (central Pacific)	228	207
Cluster 4 (west Pacific/Eurasia)	134	219

However, their net contribution is much smaller than the advection of intraseasonal moisture by the intraseasonal wind (Fig. 14a). The advection of synoptic moisture by the synoptic wind has a strong negative contribution to the total moisture advection throughout the transition period. However, leading up to the positive transition, this negative contribution weakens (Fig. 14a). The opposite scenario describes drought decay (Fig. 14b).

The advection of intraseasonal moisture by the intraseasonal wind also has the largest net change across negative transitions (Fig. 14b). It is positive and reaches a maximum 12 days prior to the transition event before rapidly decreasing to negative values across the transition. This coincides with a rapid decrease in the total moisture advection (Fig. 14b). The advection of intraseasonal moisture by the low-frequency wind also significantly contributes to the decrease in total moisture advection across the transition, reaching a minimum 7 days prior to the transition. Again, the advection of
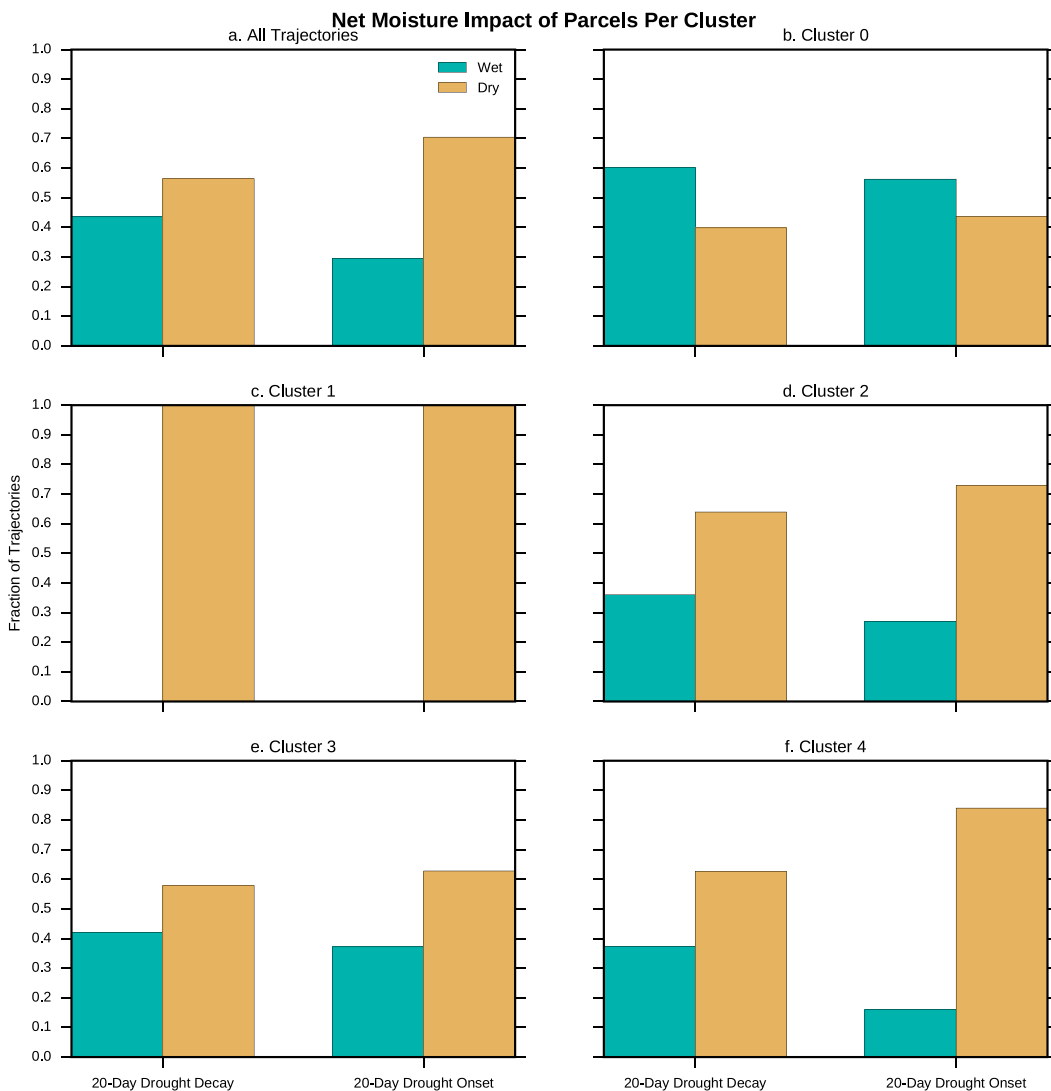

FIG. 10. The net moisture impact (a) of each trajectory (b)–(f) for each cluster is quantified for both 20-day drought decay and onset.
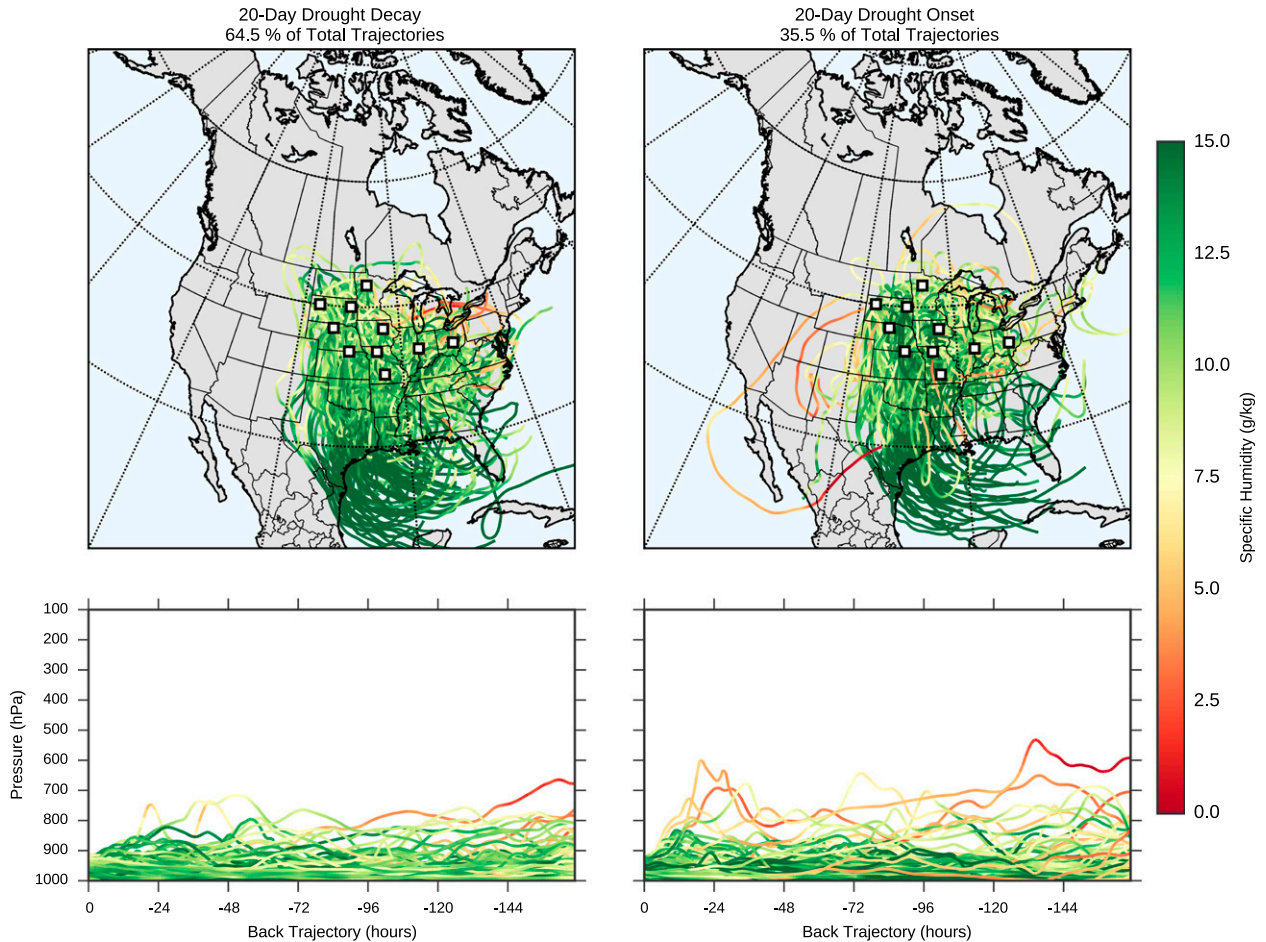
Cluster 0, 168 HH Back Trajectory

FIG. 11. Parcel trajectories from cluster 0 for both 20-day drought (left) decay and (right) onset transitions are presented, colored by the parcels specific humidity with red colors indicating lower specific humidity and green colors indicating higher specific humidity. (top) The geographic evolution of each parcel, and (bottom) their vertical travel.

synoptic moisture by the synoptic wind has a net negative contribution across the entire period, but unlike during drought decay, it does not become less negative (Fig. 14b). The linearly decomposed convergence terms reveal that the low-frequency wind and intraseasonal and synoptic moisture gradients play important roles in the change in total convergence of moisture during drought onset and decay.

In the case of 20-day drought decay, the total convergence switches from negative to positive across the transition period (Fig. 15a). Throughout the transition period, low-frequency moisture convergence by the low-frequency wind is negative (Fig. 15a). This is true during both drought onset and decay, and the term is largely indistinguishable between the two directions of transition. This result suggests that changes in low-frequency convergence of low-frequency moisture do not drive transition periods, but that such low-frequency patterns

might favor transitions in either direction. The largest differences instead come from the convergence of low-frequency moisture by the synoptic and intraseasonal wind. A regime shift occurs in both terms during drought decay, from a divergent scenario before to a convergent scenario after the transition. This regime shift coincides nicely with the rapid shift in divergent flow over the CBR, to convergent flow after the transition (Figs. 1 and 2). The opposite case is true during drought onset, with the same terms dominating the total convergence.

7. Conclusions

This study concludes several key findings that aid in the understanding of the dynamics associated with 20- and 60-day transitions toward and away from agricultural drought over the CBR. We conclude that the low-frequency pattern over the Western Hemisphere

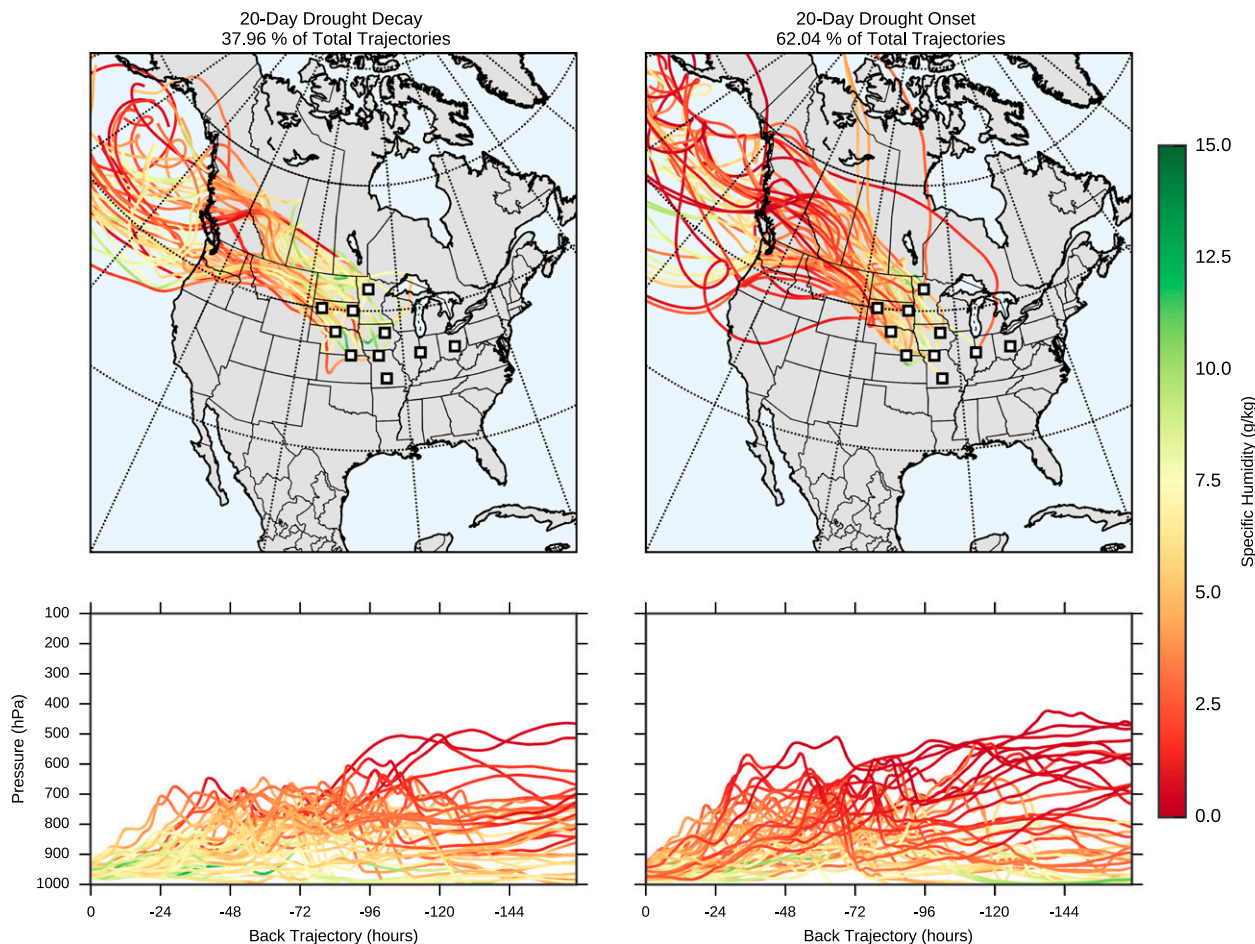**Cluster 4, 168 HH Back Trajectory**

FIG. 12. As in Fig. 11, but for cluster 4.

identified in the 20-day drought onset and decay low-frequency composites (Fig. 3) support transitions of either type. The results demonstrate that 20-day drought onset or decay transitions are more likely to occur while this low-frequency pattern is active. This conclusion can aid in assessing the seasonal risk of experiencing drought onset or decay over the CBR, in real time. There is slightly more disagreement between the 200-hPa low-frequency base states associated with 60-day drought onset and decay (Fig. 3). Still, the low-frequency base states occurring during 60-day transitions do not change substantially across the composite event. Similar to Hoerling et al. (2014) and Kumar et al. (2013), this result yields the conclusion that intraseasonal and synoptic dynamics (e.g., natural weather variability) dominate 20- and 60-day agricultural drought transitions.

The amplification of an intraseasonal wave train drives 20- and 60-day drought onset and decay (Figs. 4 and 5). During 20-day drought decay, the amplification

of this wave train coincides with a convectively coupled wave in the tropics that slowly propagates westward and that is 180° out of phase with 20-day drought onset (Fig. 6). The westward-propagating tropical wave is likely forced by extratropical wave breaking into the tropics over the central Pacific Ocean (Matthews and Kiladis 1999; MacRitchie and Roundy 2016; Sakaeda and Roundy 2015; Gloeckler and Roundy 2013). This wave amplifies and its convection apparently feeds back on the extratropical circulation, resulting in different extratropical outcomes between the two transition types, where the convection is largely out of phase (Fig. 6). Chen and Newman (1998) concluded a similar result, that convection in the western Pacific was the origin of extratropical circulations relevant to the development of the 1998 U.S. drought. Schubert et al. (2011) demonstrated similar patterns in the intraseasonal extratropical circulation as well. This feedback pattern could be a useful tool in diagnosing 20-day

10 Day Accumulated Vertically Integrated Moisture Advection and Convergence
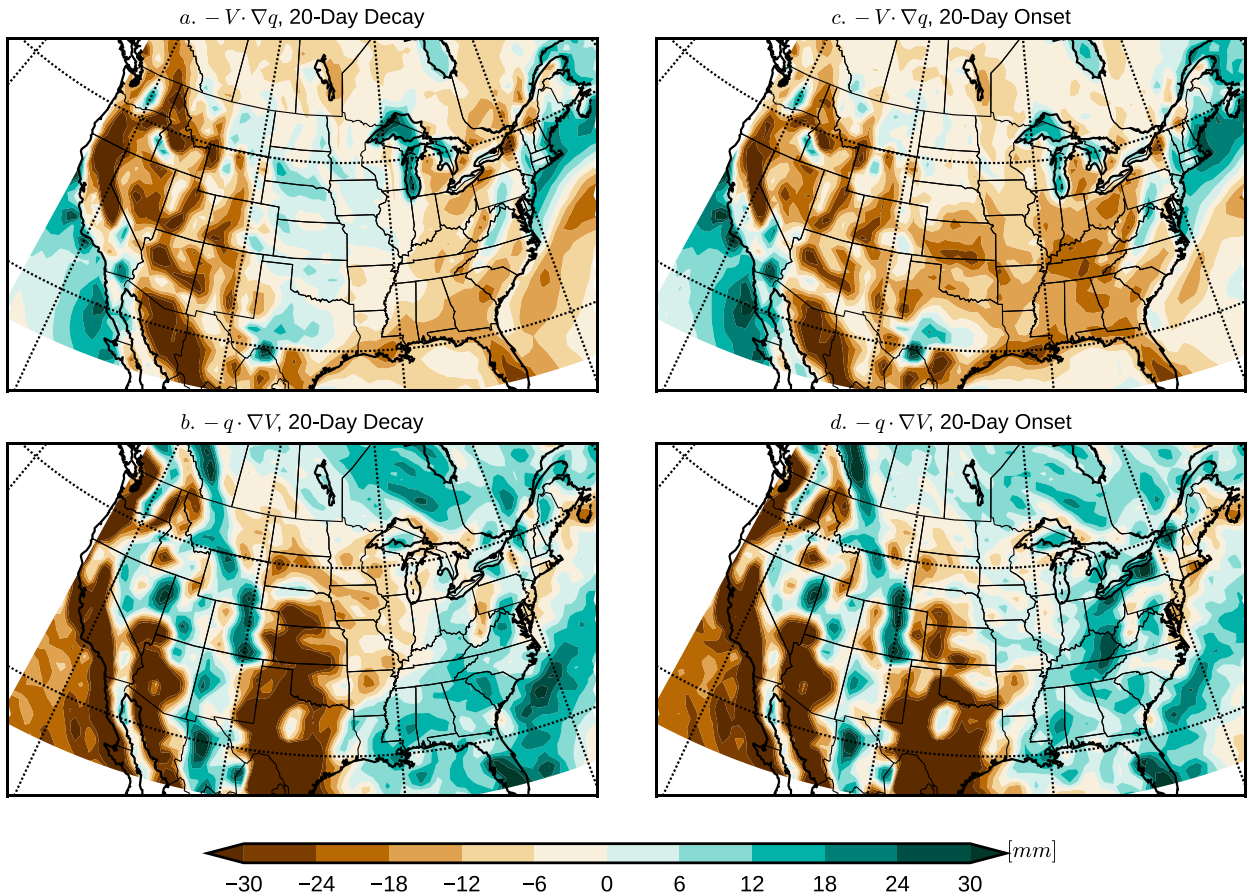

FIG. 13. Accumulated (a),(c) advection and (b),(d) convergence 10 days leading up to the transition event for 20-day drought (left) decay and (right) onset transition events.

agricultural onset or decay in real time. We note differences in the phase speed of a coherent eastward-propagating tropical wave during 60-day drought onset and decay, which is motivation for future work (Fig. 8).

Second, through a cluster analysis of parcel trajectories, we demonstrate that parcels originate in similar geographical regions leading up to drought onset and decay (Fig. 9). The main difference between the two transition types stems from the characteristics of the low-level moisture transported into the CBR from each source region, and the volume of trajectories originating from each source region (Table 2, Fig. 10). Drought decay tends to have more parcels originate over the Gulf of Mexico compared to drought onset (Table 2), leading to more moisture being transported into the CBR (Fig. 11). This is roughly consistent with Dirmeyer and Kinter (2010). In source regions where drought onset and decay events have a similar number of samples, the moisture characteristics of the parcels tend to be different (Fig. 10). That is, parcels originating in these

regions during drought decay tend to retain their moisture, while parcels originating in these regions during drought onset tend to ascend and then descend along their trajectories, thereby bringing drier air to the CBR (Fig. 13). Therefore, in the CBR, changes in surface fluxes alone are insufficient to explain agricultural drought onset and decay, because the moisture characteristics of parcels being transported into the region must be considered.

Finally, we show that the largest contributions to the change in moisture advection and convergence across transition periods are due to changes in intraseasonal moisture transport and convergence, and not to changes in low-frequency moisture transport (Figs. 14 and 15). Changes in moisture convergence and divergence are primarily driven by changes in the intraseasonal and synoptic winds and moisture gradients that subsequently affect low-frequency moisture convergence (Fig. 15).

We conclude that substantial improvements in prediction of agricultural drought onset and decay would

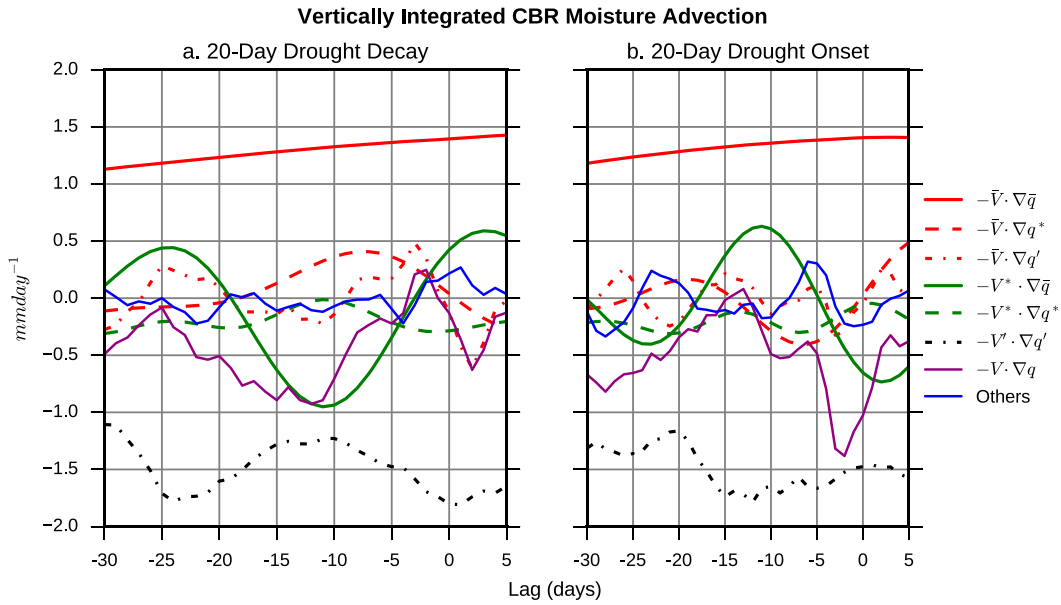**Vertically Integrated CBR Moisture Advection**

FIG. 14. Linearly decomposed moisture advection for 20-day drought (a) decay and (b) onset transition over the CBR. A 5-day centered moving average is applied to each term.

require improvement in prediction of synoptic and intraseasonal weather events. Until substantial improvements in these areas are made, drought development and termination will continue to be poorly forecast. Further, since intraseasonal and synoptic variability are not well simulated in climate models (Lin et al. 2006), it is difficult to draw conclusions about climate trends in agricultural drought over the CBR from climate models. We recommend that studies trying to assess these future trends in drought analyze trends in weather systems relevant to drought onset and decay in order to gain more confidence in the outcomes proposed.

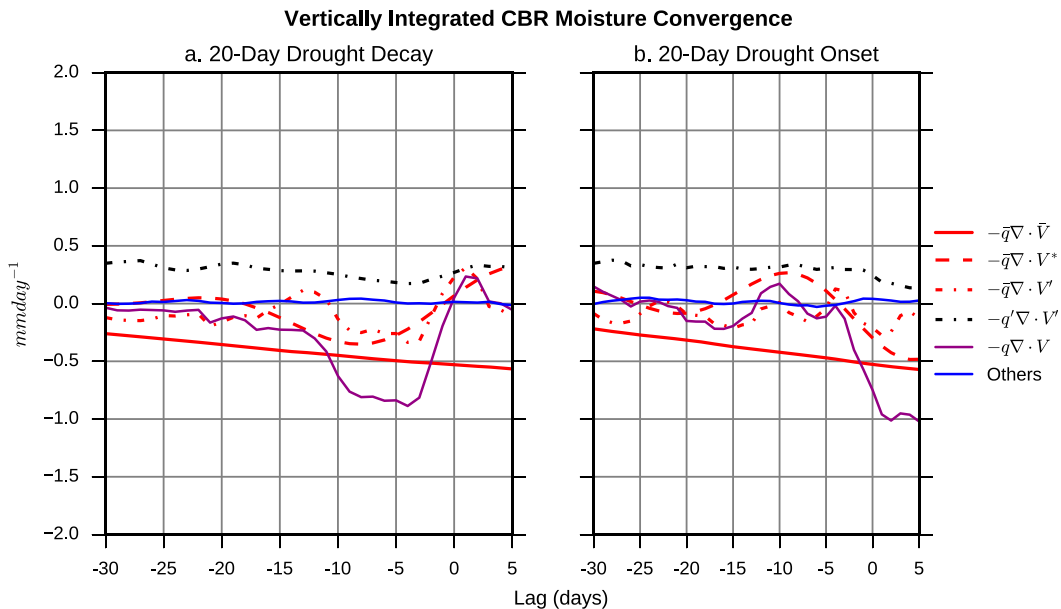**Vertically Integrated CBR Moisture Convergence**

FIG. 15. As in Fig. 14, but linearly decomposed convergence is plotted.

REFERENCES

American Meteorological Society, 2015: Agricultural drought. Glossary of Meteorology. [Available online at http://glossary.ametsoc.org/wiki/Agricultural_drought.]

Berrisford, P., and Coauthors, 2011: The ERA-Interim archive, version 2.0. ERA Report Series, ERA Rep. Series 1, ECMWF, 23 pp. [Available online at http://www.ecmwf.int/sites/default/files/elibrary/2011/8174-era-interim-archive-version-20.pdf.]

Chen, M., W. Shi, P. Xie, V. B. S. Silva, V. E. Kousky, R. W. Higgins, and J. E. Janowiak, 2008: Assessing objective techniques for gauge-based analyses of global daily precipitation. J. Geophys. Res., 113, D04110, doi:10.1029/2007JD009132.

Chen, P., and M. Newman, 1998: Rossby wave propagation and the rapid development of upper-level anomalous anticyclones during the 1988 U.S. drought. J. Climate, 11, 2491–2504, doi:10.1175/1520-0442(1998)011<2491:RWPATR>2.0.CO;2.

Cook, B. I., R. L. Miller, and R. Seager, 2009: Amplification of the North American "Dust Bowl" drought through human-induced land degradation. Proc. Natl. Acad. Sci. USA, 106, 4997–5001, doi:10.1073/pnas.0810200106.

Dai, A., 2011: Drought under global warming: A review. WIREs Climate Change, 2, 45–65, doi:10.1002/wcc.81.

Dee, D. P., and Coauthors, 2011: The ERA-Interim reanalysis: Configuration and performance of the data assimilation system. Quart. J. Roy. Meteor. Soc., 137, 553–597, doi:10.1002/qj.828.

Ding, Q., and B. Wang, 2005: Circumglobal teleconnection in the Northern Hemisphere summer. J. Climate, 18, 3483–3505, doi:10.1175/JCLI3473.1.

Dirmeyer, P. A., and J. L. Kinter, 2010: Floods over the U.S. Midwest: A regional water cycle perspective. J. Hydrometeor., 11, 1172–1181, doi:10.1175/2010JHM1196.1.

ECMWF, 2009: ERA-Interim project. National Center for Atmospheric Research Computational and Information Systems Laboratory Research Data Archive, accessed 12 January 2016, doi:10.5065/D6CR5RD9.

Frankignoul, C., and N. Sennéchael, 2007: Observed influence of North Pacific SST anomalies on the atmospheric circulation. J. Climate, 20, 592–606, doi:10.1175/JCLI4021.1.

Giannini, A., R. Saravanan, and P. Chang, 2003: Oceanic forcing of Sahel rainfall on interannual to interdecadal time scales. Science, 302, 1027–1030, doi:10.1126/science.1089357.

Gloeckler, L. C., and P. E. Roundy, 2013: Modulation of the extratropical circulation by combined activity of the Madden–Julian oscillation and equatorial Rossby waves during boreal winter. Mon. Wea. Rev., 141, 1347–1357, doi:10.1175/MWR-D-12-00179.1.

Heim, R. R., 2002: A review of twentieth-century drought indices used in the United States. Bull. Amer. Meteor. Soc., 83, 1149–1165, doi:10.1175/1520-0477(2002)083<1149:AROTDI>2.3.CO;2.

Hoerling, M., and A. Kumar, 2003: The perfect ocean for drought. Science, 299, 691–694, doi:10.1126/science.1079053.

——, J. Eischeid, A. Kumar, R. Leung, A. Mariotti, K. Mo, S. Schubert, and R. Seager, 2014: Causes and predictability of the 2012 great plains drought. Bull. Amer. Meteor. Soc., 95, 269–282, doi:10.1175/BAMS-D-13-00055.1.

Huang, C., S. Duiker, L. Deng, C. Fang, and W. Zeng, 2015: Influence of precipitation on maize yield in the eastern United States. Sustainability, 7, 5996–6010, doi:10.3390/su7055996.

Kumar, A., M. Chen, M. Hoerling, and J. Eischeid, 2013: Do extreme climate events require extreme forcings? Geophys. Res. Lett., 40, 3440–3445, doi:10.1002/grl.50657.

Lau, N. C., 1997: Interactions between global SST anomalies and the midlatitude atmospheric circulation. Bull. Amer. Meteor. Soc., 78, 21–33, doi:10.1175/1520-0477(1997)078<0021:IBGSAA>2.0.CO;2.

Lee, H.-T., 2014: Climate Algorithm Theoretical Basis Document (C-ATBD): Outgoing Longwave Radiation (OLR)—Daily. NOAA's Climate Data Record (CDR) Program, CDRP-ATBD-0526, 46 pp. [Available online at http://www1.ncdc.noaa.gov/pub/data/sds/cdr/CDRs/Outgoing%20Longwave%20Radiation%20-%20Daily/AlgorithmDescription.pdf.]

Lin, J.-L., and Coauthors, 2006: Tropical intraseasonal variability in 14 IPCC AR4 climate models. Part I: Convective signals. J. Climate, 19, 2665–2690, doi:10.1175/JCLI3735.1.

Lorenz, E. N., 1963: Deterministic nonperiodic flow. J. Atmos. Sci., 20, 130–141, doi:10.1175/1520-0469(1963)020<0130:DNF>2.0.CO;2.

MacRitchie, K., and P. E. Roundy, 2016: The two-way relationship between the Madden–Julian oscillation and anticyclonic wave breaking. Quart. J. Roy. Meteor. Soc., 142, 2159–2167, doi:10.1002/qj.2809.

Matthews, A. J., and G. N. Kiladis, 1999: The tropical–extratropical interaction between high-frequency transients and the Madden–Julian Oscillation. Mon. Wea. Rev., 127, 661–677, doi:10.1175/1520-0493(1999)127<0661:TTEIBH>2.0.CO;2.

Mo, K. C., and J. E. Schemm, 2008: Droughts and persistent wet spells over the United States and Mexico. J. Climate, 21, 980–994, doi:10.1175/2007JCLI1616.1.

Namias, J., 1955: Some meteorological aspects of drought with special reference to the summers of 1952–54 over the United States. Mon. Wea. Rev., 83, 199–205, doi:10.1175/1520-0493(1955)083<0199:SMAOD>2.0.CO;2.

NOAA/OAR/ESRL PSD, 2016: CPC U.S. Unified Precipitation Dataset. Boulder, CO, accessed 12 January 2016. [Available online at http://www.esrl.noaa.gov/psd/.]

Piechota, T. C., and J. A. Dracup, 1996: Drought and regional hydrologic variations in the United States: Associations with the El Niño–Southern Oscillation. Water Resour. Res., 32, 1359–1373, doi:10.1029/96WR00353.

Rajagopalan, B., E. Cook, U. Lall, and B. K. Ray, 2000: Spatiotemporal variability of ENSO and SST teleconnections to summer drought over the United States during the twentieth century. J. Climate, 13, 4244–4255, doi:10.1175/1520-0442(2000)013<4244:SVOEAS>2.0.CO;2.

Riddle, E. E., M. B. Stoner, N. C. Johnson, M. L. L'Heureux, D. C. Collins, and S. B. Feldstein, 2013: The impact of the MJO on clusters of wintertime circulation anomalies over the North American region. Climate Dyn., 40, 1749–1766, doi:10.1007/s00382-012-1493-y.

Rousseeuw, P. J., 1987: Silhouettes: A graphical aid to the interpretation and validation of cluster analysis. J. Comput. Appl. Math., 20, 53–65, doi:10.1016/0377-0427(87)90125-7.

Sakaeda, N., and P. E. Roundy, 2015: The development of upper-tropospheric wind over the Western Hemisphere in association with MJO convective initiation. J. Atmos. Sci., 72, 3138–3160, doi:10.1175/JAS-D-14-0293.1.

Schubert, S. D., M. J. Suarez, P. J. Pegion, R. D. Koster, and J. T. Bacmeister, 2004a: Causes of long-term drought in the U.S. Great Plains. J. Climate, 17, 485–504, doi:10.1175/1520-0442(2004)017<0485:COLDIT>2.0.CO;2.

——, ——, ——, ——, and ——, 2004b: On the cause of the 1930s Dust Bowl. Science, 303, 1855–1859, doi:10.1126/science.1095048.

——, ——, ——, ——, and ——, 2008: Potential predictability of long-term drought and pluvial conditions in the U.S.

Great Plains. *J. Climate*, **21**, 802–816, doi:10.1175/2007JCLI1741.1.

——, and Coauthors, 2009: A U.S. CLIVAR project to assess and compare the responses of global climate models to drought-related SST forcing patterns: Overview and results. *J. Climate*, **22**, 5251–5272, doi:10.1175/2009JCLI3060.1.

——, H. Wang, and M. Suarez, 2011: Warm season subseasonal variability and climate extremes in the Northern Hemisphere: The role of stationary Rossby waves. *J. Climate*, **24**, 4773–4792, doi:10.1175/JCLI-D-10-05035.1.

Seager, R., 2007: The turn of the century North American drought: Global context, dynamics, and past analogs. *J. Climate*, **20**, 5527–5552, doi:10.1175/2007JCLI1529.1.

——, and N. Henderson, 2013: Diagnostic computation of moisture budgets in the ERA-interim reanalysis with reference to analysis of CMIP-archived atmospheric model data. *J. Climate*, **26**, 7876–7901, doi:10.1175/JCLI-D-13-00018.1.

——, and Coauthors, 2007: Model projections of an imminent transition to a more arid climate in southwestern North America. *Science*, **316**, 1181–1184, doi:10.1126/science.1139601.

——, Y. Kushnir, M. Ting, M. Cane, N. Naik, and J. Miller, 2008: Would advance knowledge of 1930s SSTs have allowed prediction of the Dust Bowl drought? *J. Climate*, **21**, 3261–3281, doi:10.1175/2007JCLI2134.1.

Stein, A., R. Draxler, G. Rolph, B. Stunder, M. Cohen, and F. Ngan, 2015: NOAA's HYSPLIT Atmospheric Transport and Dispersion Modeling System. *Bull. Amer. Meteor. Soc.*, **96**, 2059–2077, doi:10.1175/BAMS-D-14-00110.1.

Ting, M., and H. Wang, 1997: Summertime U.S. precipitation variability and its relation to Pacific sea surface temperature. *J. Climate*, **10**, 1853–1873, doi:10.1175/1520-0442(1997)010<1853:SUSPVA>2.0.CO;2.

Trenberth, K. E., and C. J. Guillemot, 1996: Physical processes involved in the 1988 drought and 1993 floods in North America. *J. Climate*, **9**, 1288–1298, doi:10.1175/1520-0442(1996)009<1288:PPIITD>2.0.CO;2.

Wilhite, D. A., Ed., 2000: Drought as a natural hazard: Concepts and definitions. *Drought: A Global Assessment*, Vol. 1, Routledge Publishers, 3–18.

Wu, R., and J. L. Kinter, 2009: Analysis of the relationship of U.S. droughts with SST and soil moisture: Distinguishing the time scale of droughts. *J. Climate*, **22**, 4520–4538, doi:10.1175/2009JCLI2841.1.

Zhang, C., 2005: Madden–Julian Oscillation. *Rev. Geophys.*, **43**, RG2003, doi:10.1029/2004RG000158.